Available online at www.sciencedirect.com

ScienceDirect

journal homepage: www.elsevier.com/locate/he

One-pot synthesis of pure phase molybdenum carbide (Mo_2C and MoC) nanoparticles for hydrogen evolution reaction

Sanjay Upadhyay, O.P. Pandey *

School of Physics and Materials Science, Thapar Institute of Engineering & Technology, Patiala, 147004, India

HIGHLIGHTS

- Mo_2C particles embedded in graphitic carbon: an effective electrocatalyst for HER.
- Comparison of electrochemical performance of Mo_2C and MoC.
- Effect of reaction parameters on the formation of pure phase Mo_2C and MoC.
- Cost-effective method to prepare Mo_2C and MoC in a single step.

GRAPHICAL ABSTRACT

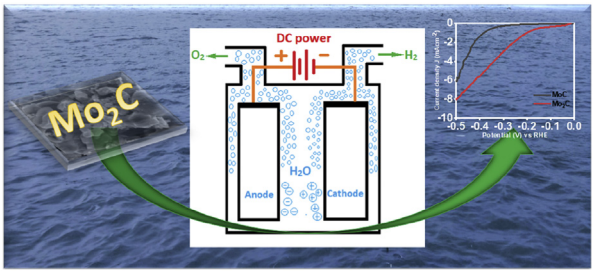

ARTICLE INFO

Article history:
Received 12 June 2020
Received in revised form
5 July 2020
Accepted 7 July 2020
Available online 28 July 2020

Keywords:
Molybdenum carbide
One-pot synthesis
Carbon-coated
Electrocatalyst
Hydrogen evolution reaction
Capacitance

ABSTRACT

Herein, we report the one-step synthesis of pure phase molybdenum carbide (Mo_2C and MoC) nanoparticles via the in-situ carburization reduction route without using any reducing agent. The X-ray diffraction (XRD) results confirm the formation of pure phase Mo_2C and MoC at 800 °C for 8 h and 15 h respectively. The as-synthesized powders have been investigated for hydrogen production and energy storage applications. The pure phase Mo_2C shows high performance towards the hydrogen evolution reaction (HER) with a Tafel slope of 129.7 mV dec^{-1} however, MoC exhibits a low activity towards HER with a Tafel slope of 266 mV dec^{-1}. Both the phases show high stability up to 5000 cyclic voltammetry (CV) cycles in the potential range of 0–0.4 V. In the case of MoC, the specific capacitance increases during the initial 2000 CV cycles which may be attributed to the electrode activation during the CV test. The Mo_2C powder shows a double layer capacitance (C_{dl}) value of 2.47 mF cm^{-2} and a specific capacitance of 2.24 mF g^{-1}. The MoC phase shows a higher C_{dl} value of 8.99 mF cm^{-2} and a specific capacitance of 8.17 mF g^{-1}.

* *Corresponding author.*
E-mail address: oppandey@thapar.edu (O.P. Pandey).
https://doi.org/10.1016/j.ijhydene.2020.07.069

Introduction

The ever-increasing fossil fuel consumption and associated environmental issues trigger the requirement of renewable and environment-friendly energy sources. Hydrogen has been found to be a good replacement to conventional fossil fuels due to its high energy density. Moreover, it does not produce any harmful byproducts [1,2]. Hydrogen exists on earth in abundance but not as a free molecule. Electrochemical water splitting can produce hydrogen at a very low cost through the hydrogen evolution reaction (HER) [3,4]. This process requires an electrocatalyst having high activity, high surface area, and high stability to decrease the overpotential for improving efficiency [5,6]. The conventional platinum (Pt) shows the highest catalytic activity towards HER, up to date. However, the high cost and low abundance limit its uses on a large scale [7]. This puts pressure on the scientific community to develop such kind of materials which can replace the precious platinum [8].

Many electrocatalysts with an outstanding electrochemical performance for HER have been reported recently [9–12]. Molybdenum is much more abundant in nature than noble metals such as Pt. Molybdenum based compounds are found to be highly active towards HER and have the potential for replacing precious Pt [13,14]. However, molybdenum alloys such as Ni–Mo exhibit less stability in acidic media [15,16]. Therefore, molybdenum-based compounds such as carbides, nitrides, sulfides, selenides, etc. are being investigated as an electrocatalyst because they are highly stable in acidic media. Among these compounds, molybdenum carbides have been found as a good replacement to platinum because of its excellent catalytic activity and high stability in acidic and basic mediums [17–23]. The Mo_2C phase was found to be highly active towards HER than the other phases due to its special electronic structure which is similar to the electronic states of Pt [24–26]. The catalytic activity of Mo_2C and MoC has been studied previously using Density Functional Theory (DFT) calculations. It was found that, among the existing phases of molybdenum carbide, Mo_2C has a stronger metallic character and exhibits the strongest covalent bond. Also, Mo_2C has a low work function of only 3.4 eV, which suggests that it is appropriate for electrocatalysis [27]. Also, if the Mo_2C particles are encapsulated inside carbon layers, the electrochemical activity and stability of the particles are enhanced [28–30].

The synthesis processes for Mo_2C has been improved significantly after a few years of research. Dong et al. reported cost-effective Mo rich Mo_2C in two-step synthesis exhibiting high catalytic activity with a low overpotential of 67 mV and a low Tafel slope of 55 mV dec^{-1} [31]. Zhao et al. synthesized nanocrystals of Mo_2C embedded in the carbon layers by hydrothermal method, which showed overpotential of 170 mV in acidic and 119 mV in basic media for 10 mA dec^{-1} current density [32]. Pan at el. developed a two-step method to synthesize Mo_2C supported by carbon layers on reduced graphene oxide (Mo_2C-RGO). The synthesized hybrid (Mo_2C-RGO) showed high catalytic activity towards HER with a Tafel slope of 54 mV dec^{-1} and an overpotential of 70 mV at 10 mA dec^{-1} current density [33]. Xia et al. studied the HER performance of Mo_2C nanoparticles supported on nitrogen-doped carbon nanosheets. It exhibited high performance towards HER with a low overpotential of 130 mV in acidic and 108 mV in basic media at a current density of 10 mA dec^{-1} [34].

In short, up to date, all the above reported methods for synthesizing Mo_2C typically include multistep and/or complex synthesis procedures that are environmentally unfriendly and/or expensive. These flaws will hinder their use on a global scale [29]. Moreover, the reported materials were synthesized under different synthesis conditions for achieving better electrochemical properties from Mo_2C and higher specific capacitance from MoC.

Herein, we report a cost-effective and eco-friendly method to synthesize pure phase Mo_2C and MoC embedded in graphitic carbon in a single step via the in-situ carburization reduction route. During the synthesis, no external reducing agent has been used. Many researchers reported the synthesis of Mo_2C and MoC under different synthesis conditions and their electrochemical activity was investigated [35–38]. In this work, pure phase Mo_2C and MoC have been synthesized under similar experimental conditions by varying the reaction parameters and their electrochemical properties have been compared. The Mo_2C particles were encapsulated inside the graphitic carbon, which enhances the stability and activity for HER. However, the highly ordered graphic layers in the MoC powder improves the electrochemical capacitance and stability. The cyclic stability test up to 3000 CV cycles of Mo_2C and MoC has been done by many groups [39–41]. However, in the present work both the phases exhibited long cycle stability up to 5000 CV cycles. The 5000 CV cycle took about 10 h to complete. The Mo_2C showed high electrocatalytic activity towards HER with a low Tafel slope of 129.7 mV dec^{-1} in the acidic medium [37,42,43]. However, MoC showed a Tafel slope of 266 mV dec^{-1}. Also, Mo_2C and MoC exhibited a specific capacitance of 2.24 mF g^{-1} and 8.17 mF g^{-1} respectively. The present synthesis method showed promising potential to synthesize noble metal-free electrocatalyst at a very low price.

Experimental section

Synthesis

For the synthesis of pure phase Mo_2C and MoC, ammonium molybdenum tetrahydrate ($(NH_4)_6Mo_7O_{24} \cdot 4H_2O$) was taken as a molybdenum source and hexamethylenetetramine ($C_6H_{12}N_4$) was used as a carbon source. In this work, 1.235 g of ammonium molybdenum tetrahydrate (AHM) and 1.401 g of Hexamethylenetetramine (HMT) were mixed in an agate mortar and transferred into a specially designed stainless-steel autoclave and sealed properly. The autoclave was placed inside a pot furnace and the temperature was raised from room temperature to 700, 800, and 900 °C at a constant heating rate of 5 °C per minute for 10 h. In the second set of experiments, the temperature was maintained at 800 °C for 6, 8, 10, 12, and 15 h of holding time with the same molar ratio of precursors. To obtain the pure phase Mo_2C, the third set of experiments were done in which the molar ratio of precursors was varied from 1:10 to 1:12 and 1:14 at a reaction temperature of 800 °C for 8 h. At last, the autoclave was allowed to cool to

room temperature and the obtained black powder was collected. The details of the reaction parameters during experiments and phases obtained are shown in Table 1.

Characterization

The synthesized powders were characterized by XRD for phase formation and structural analysis via PANalytical X-Pert-Pro diffractometer having CuKα radiation (λ = 1.5406 Å) by copper target with an inbuilt Nickel filter. All the XRD patterns were taken at room temperature between $20^{\circ} \leq 2\theta \leq 80^{\circ}$. X-Pert High Score Plus was used for phase identification by matching the patterns with the ICDD database. The morphological and microstructural studies were done using Field emission scanning electron microscopy (JEOL JSM 5600) and (TEM) transmission electron microscopy (JEOL 2100F) operating at 15 kV and 200 kV respectively. X-ray photoelectron spectroscopy measurements were done using AlKα (1486.6 eV) radiation operating at 15 kV and 15 mA. The degree of graphitization was estimated by Raman spectroscopy via Jobin Yvon Horibra LABRAM-HR 800 with a laser light of 473 nm at room temperature.

Electrochemical studies

The electrochemical studies of as-prepared powders towards HER were done in a three-electrode cell assembly of biologic EC lab instrument (SP-300). The working electrode was prepared using the following procedure.

1.5 mg of the synthesized powder was mixed in 250 μl of ethanol and the solution was sonicated for 30 min to disperse the particles uniformly. In the obtained solution, 60 μl Nafion 117 (Sigma Aldrich) solution was mixed and sonicated for 10 min 20 μl of the solution was dropped onto the top surface of the glassy carbon electrode (GCE) having a surface area of 0.070 cm^2. Finally, the GCE was left overnight at room temperature for drying.

All the measurements were done using reversible hydrogen electrode (RHE) and platinum electrode as reference and counter electrode respectively. In a 0.5 M H_2SO_4 electrolyte solution, all the electrodes were immersed. The linear sweep voltammetry (LSV) measurements were performed between 0.1 V and 0.6 V at a scan rate of 5 mV s^{-1}. The cyclic voltammetry (CV) plots were measured at a scan rate of 100 mV s^{-1} for 5000 cycles in a voltage range of 0–0.4 V. CV curves at multiple scan rates were taken in the same potential range (0–0.4 V) to estimate of EDLC measurements. The galvanic charge-discharge curves were measured from 0 to 1 V at different current densities. The EIS measurements were performed within a frequency range of 10^2–10^{-2} Hz. Before recording the measurements, CV curves were performed in a voltage range of −1 V to 1 V at a scan rate of 100 mV s^{-1} to activate catalyst, remove contamination and stabilize the electrochemical current [44].

Results and discussion

XRD

The crystallographic information of the as-synthesized samples was obtained by the X-ray diffraction technique. The formation of Mo_2C and MoC occurs through the decomposition of the precursors at high temperatures. To understand the effect of reaction parameters on the phase formation, a series of samples were prepared at different reaction temperatures, reaction times, and molar ratios of precursors. Fig. 1 shows the XRD patterns of the samples synthesized at different reaction temperatures while keeping the other parameters constant. Fig. 1a–c represent the XRD patterns of the samples synthesized at reaction temperatures of 700, 800, and 900 °C respectively. In Fig. 2, the XRD patterns of the samples synthesized at different reaction time while keeping the other parameters constant are shown. Fig. 2a–e represent the XRD patterns of the samples synthesized at 6, 8, 10, 12, and 15 h of reaction times respectively. The XRD patterns of the powders synthesized at a different molar ratio of precursors while keeping the other reaction parameters constant are shown in Fig. 3. Fig. 3a–c represent the XRD patterns of the samples synthesized at a molar ratio of 1:10, 1:12, and 1:14 (Mo:C) respectively.

Effect of reaction temperature

To investigate the influence of reaction temperature on the phase formation, the samples were synthesized at 700, 800, and 900 °C of reaction temperatures at a constant reaction time of 10 h and a molar ratio of 1:10 (Mo:C). At 700 °C, AHM decomposes to MoO_2, and the intense diffraction peaks at 2θ values 26.1, 36.9, 43.4, 53.6, 60.7, and 66.8 appear, which indicates the formation of single-phase MoO_2 [45] (Fig. 1a). The decomposition of AHM follows the equation:

Table 1 – Reaction parameters, major and minor phases obtained and crystallite size.

S. No.	Temperature (°C)	Holding time (h)	Molar ratio of precursors	Phases obtained		Crystallite Size (nm)
				Major	Minor	
1.	700	10	1:10	MoO_2	—	87.68
2.	800	6	1:10	MoC	Mo_2C	15.96
3.	800	8	1:10	Mo_2C	MoC, C	120.6
4.	800	10	1:10	Mo_2C	MoC, C	38.47
5.	800	12	1:10	MoC	Mo_2C	32.63
6.	800	15	1:10	MoC	—	17.28
7.	800	8	1:12	Mo_2C	—	16.53
8.	800	8	1:14	Mo_2C	MoC	10.95
9.	900	10	1:10	Mo_2C	MoC	43.49

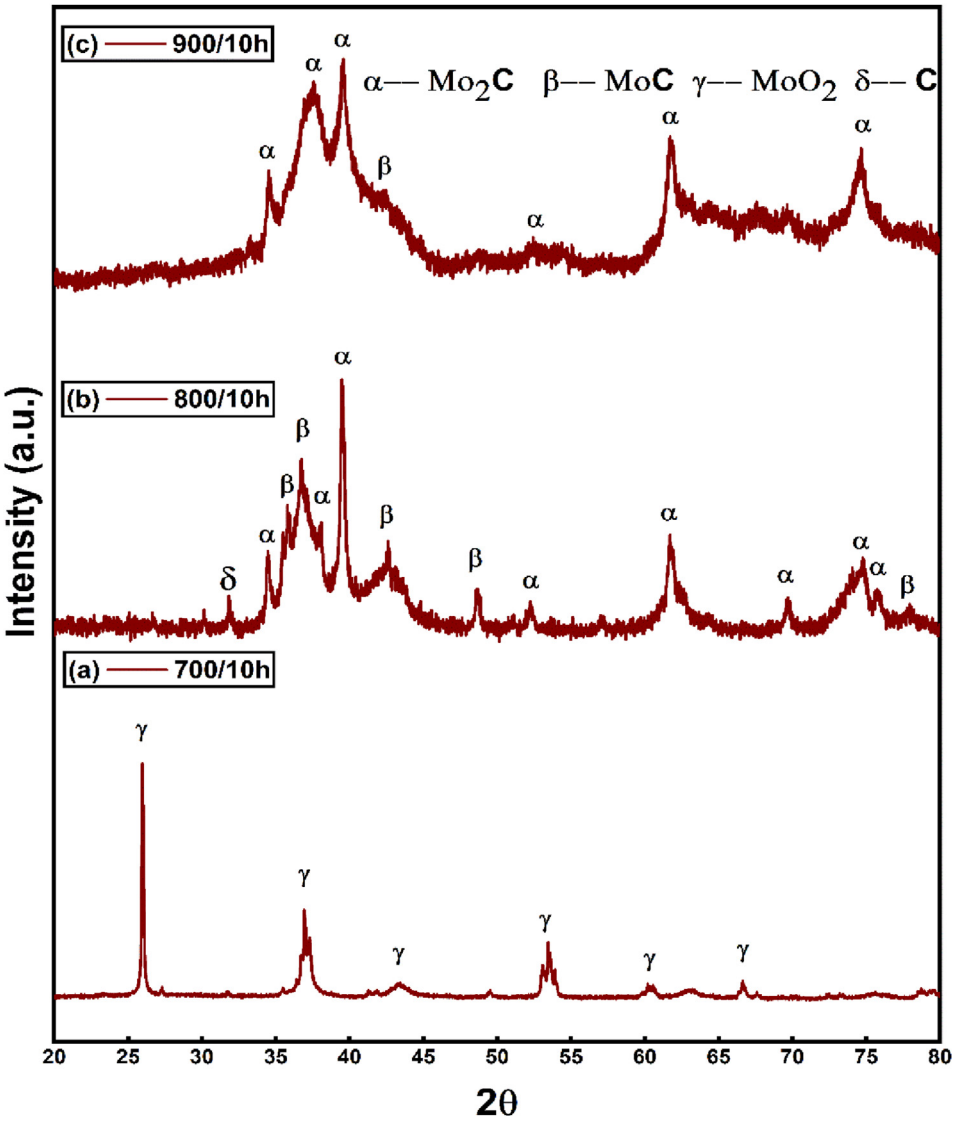

Fig. 1 – XRD patterns of the samples synthesized at different reaction temperatures.

$$(NH_4)_6Mo_7O_{24}.4H_2O \xrightarrow{\Delta} 7MoO_3 + 6NH_3 + 7H_2O \quad (1)$$

Further, the H_2 gas produced by the thermal decomposition of NH_3 ($2NH_3 \xrightarrow{\Delta} N_2 + 3H_2$) during the reaction helps in the reduction of MoO_3 to MoO_2 [46]. The reduction of MoO_3 by H_2 gas occurs by the following scheme.

$$MoO_3 + H_2 \rightarrow MoO_2 + H_2O \quad (2)$$

MoO_2 does not carburize to form the molybdenum carbide phases at this temperature. Further, the reaction temperature was increased to 800 °C and the carburization of MoO_2 begins to form Mo_2C and MoC with a vol% of 80.72 and 16.14 respectively. Excess carbon also shows its presence at 2θ value 31.89 with a vol% of 3.14 (Fig. 1b). The diffraction peaks of Mo_2C, MoC, and C can be matched with the ICDD card number (00-035-0787), (01-089-2868), and (00-018-0311) respectively. The formation of Mo_2C and MoC by the carburization of MoO_2 with HMT can be written as,

$$C_6H_{12}N_4 + 6MoO_2 \rightarrow 3Mo_2C + 6H_2O + 3CO_2 + 2N_2 \quad (3)$$

$$and\ 2C_6H_{12}N_4 + 9MoO_2 \rightarrow 9MoC + 12H_2O + 3CO_2 + 4N_2 \quad (4)$$

At 900 °C, the diffraction peaks of MoC disappears and the intense diffraction peaks of Mo_2C came into existence (Fig. 1c). Vol % of Mo_2C and MoC were calculated to be equal to 91.2 and 8.8 respectively. The crystallite size of the powders was calculated using the Debye Scherrer equation, $D = 0.9\lambda/(\beta\cos\theta)$ where 0.9 is Scherrer constant, λ is the wavelength used, β is the FWHM (radians) and θ is the angle of diffraction. Table 1 indicates that the crystallite size of the samples decreases from 87.68 to 38.47 nm when the temperature rises from 700 to 800 °C and increases from 38.47 to 43.49 nm when the temperature rises from 800 to 900 °C. The crystallite size depends

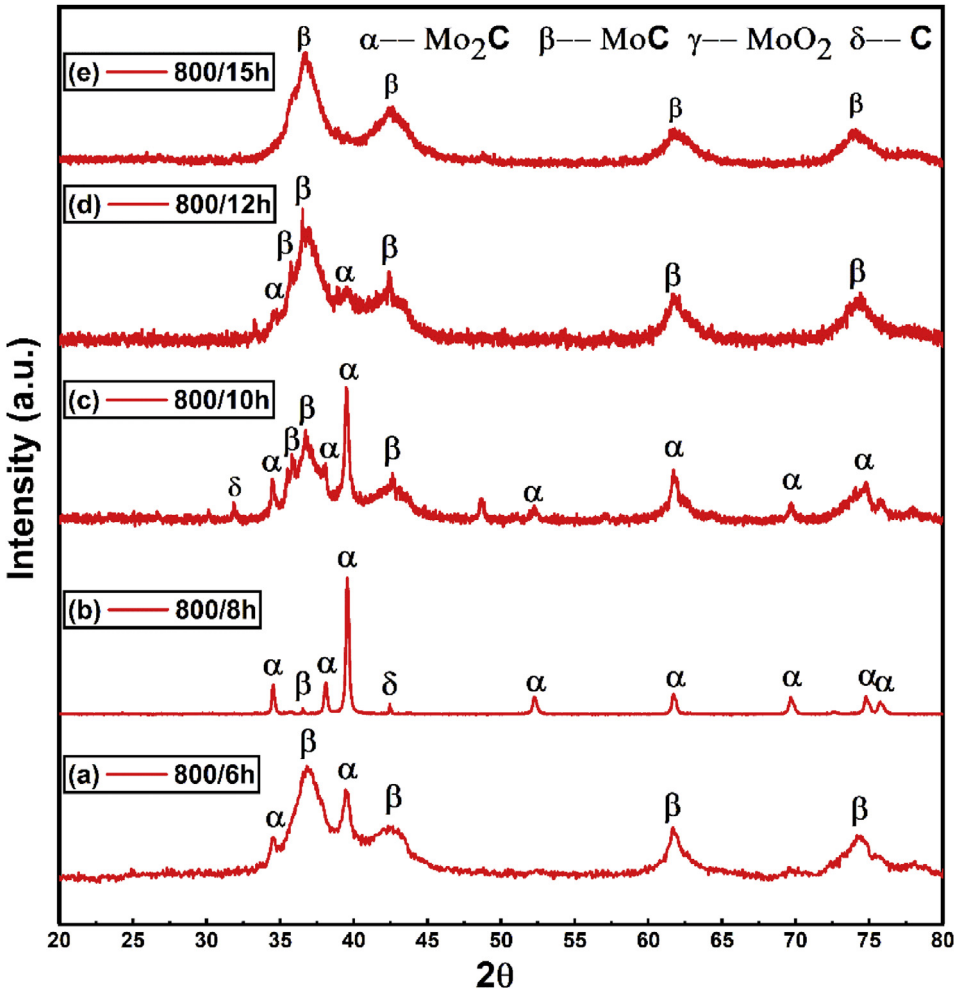

Fig. 2 – XRD patterns of the samples synthesized at different reaction times.

upon the ordering inside the material. The higher the ordering inside the material the higher will be the crystallite size and vice versa. At 700 °C, the bonds of MoO_2 break to form Mo_2C/MoC, and the order inside the material decreases, and hence crystallite size decreases. Above 800 °C, the MoC phase transforms to Mo_2C, and the order inside the powder increases, and hence crystallite size increases.

Effect of reaction time

The reaction time variation was done to optimize the synthesis conditions to obtain pure phase Mo_2C and MoC at a constant reaction temperature of 800 °C and molar ratio of 1:10 (Mo:C). Fig. 2a shows the XRD pattern of the sample synthesized at 6 h of reaction time in which the diffraction peaks of Mo_2C (8.6 vol%) and MoC (91.4 vol%) appear. However, when the holding time was increased to 8 h, the MoC phase starts transforming to Mo_2C. The volume percentage of the Mo_2C phase increases to 98.5 and the MoC phase decrease to 0.7 vol% along with excess carbon in 0.8 vol% (Fig. 2b). Further increasing the reaction time to 10 h, Mo_2C and MoC phases along with excess carbon were obtained. As discussed earlier, the vol% of Mo_2C, MoC, and C were 80.72, 16.14, and 3.14 respectively (Fig. 2c). When the reaction time was increased to 12 h, the diffraction peaks of Mo_2C and MoC phases were observed in the XRD pattern (Fig. 2d). Vol % of Mo_2C and MoC was calculated to be equal to 3.6 and 96.4 respectively. With increasing holding time to 15 h pure phase MoC was obtained (Fig. 2e) according to Eq. (4). Moreover the role of reaction time for the formation of Mo_2C and MoC has been studied previously [47]. The crystallite size increases with reaction time and after a certain time reached it decreases with increasing reaction time (Table 1). Above 4 h of reaction time, MoC transformed into highly ordered Mo_2C, and the crystallite size increases. Above 8 h of reaction time, the Mo_2C phase transforms into low ordered MoC, and therefore the crystallite size decreases.

Effect of amount of precursors

In the third set of experiments, variation in the molar ratio of precursors was done at a constant reaction temperature of 800 °C and reaction time of 8 h. As discussed above when the molar ratio was kept at 1:10 the mixed phases of Mo_2C (98.5 vol %), MoC (0.7 vol%), and C (0.8 vol%) were obtained (Fig. 3a). When the molar ratio was kept at 1:12 we get pure phase Mo_2C. In Fig. 3b, the diffraction peaks at 2θ values 34.4, 37.9, 39.5, 52.2, 61.6, 74.7, and 75.7 were observed. However, no additional peak was detected in the XRD pattern. The detected diffraction peaks are consistent with the previously reported

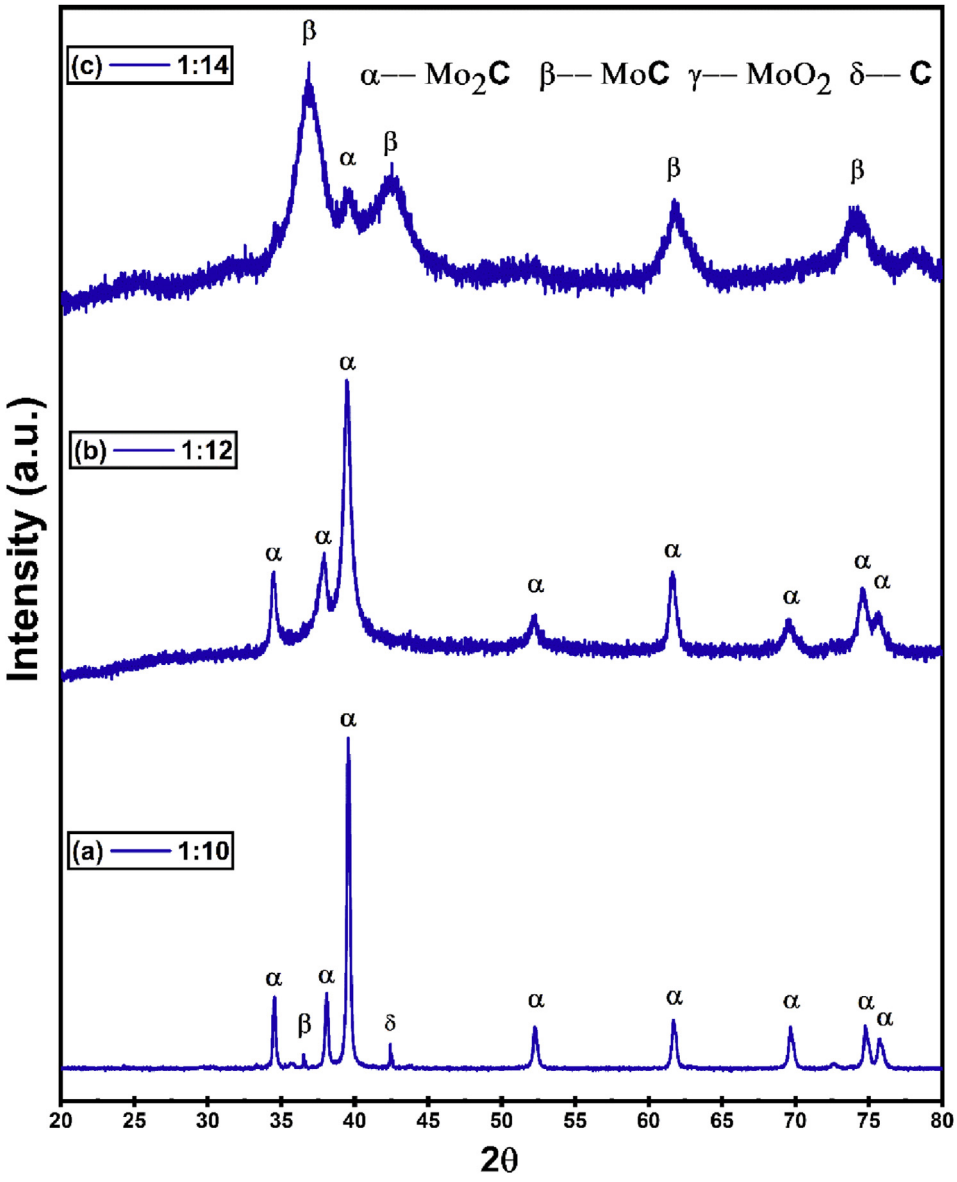

Fig. 3 – XRD patterns of the samples synthesized at different molar ratios of precursors.

Mo_2C [48]. It indicates that the obtained phase of molybdenum carbide is pure Mo_2C. Eq. (3) represents the reaction of the formation of Mo_2C. Further increasing the molar ratio to 1:14, MoC (97.2 vol%) and Mo_2C (2.8 vol%) phases were obtained (Fig. 3c). The crystallite size of the powders synthesized at different molar ratios of precursors decreases from 120.6 at 1:10 to 10.95 at 1:14. At a molar ratio of 1:10, bonds inside MoC breaks to form Mo_2C, and the order inside the powder decreases, and hence the crystallite size decreases. Further increasing the molar ratio to 1:14, Mo_2C transforms into MoC and the order inside the powder decreases and hence crystallite size decreases.

The above results reveal that Mo_2C or MoC can be obtained at a particular value of reaction temperature, time, and the molar ratio of precursors. A change in any of these three factors influences the formation of Mo_2C and MoC, which means the formation of the Mo_2C and MoC phases is a critical process.

XPS

The as-synthesized powders were further probed with X-Ray photoelectron spectroscopy to investigate its composition and surface chemical states. Fig. 4a–c show the XPS spectra of Mo_2C however, Fig. 4d–f show the XPS spectra of MoC powder. Both the survey spectrums of Mo_2C and MoC are similar (Fig. 4a and d). In the survey spectrums, the peaks positioned at 399.1, 229.2, 529.9, and 232 eV indicating the presence of Mo, O, and C elements on the surface of the samples [49]. Fig. 4b shows the deconvoluted high-resolution XPS spectra of Mo3d (Mo_2C), which can be fitted into five peaks. The peaks centered at 233.1, 235.7, and 236.4 eV are assigned to Mo^{4+} $3d_{3/2}$, Mo^{6+}

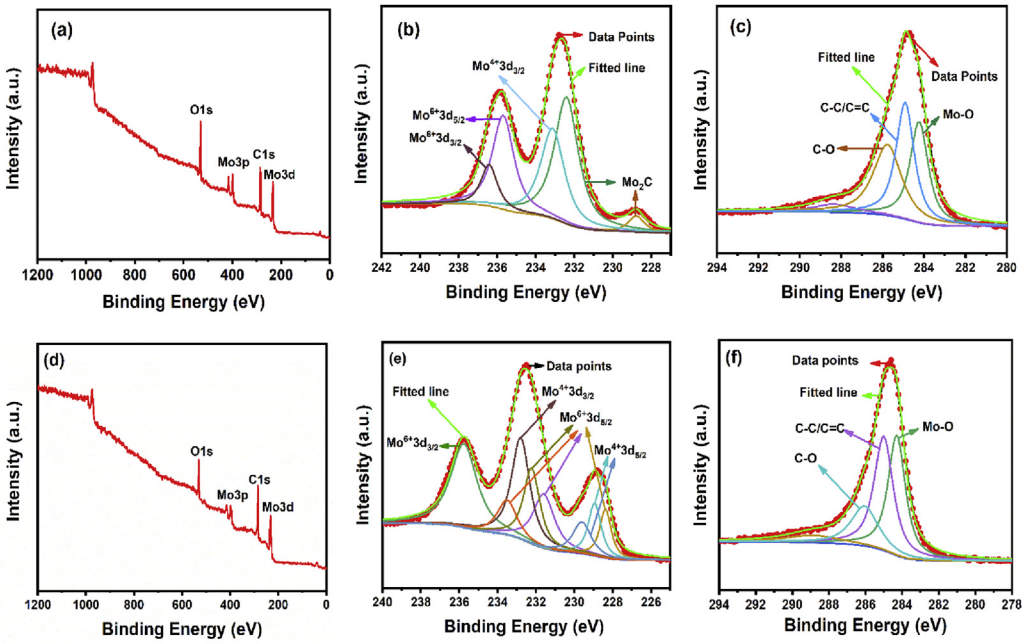

Fig. 4 – XPS spectrum of Mo_2C powder (a) Survey spectrum; high resolution spectra of (b) Mo3d, and (c) C1s of Mo_2C powder; XPS spectrum of MoC powder (d) Survey spectrum; high resolution spectra of (e) Mo3d, and (f) C1s of MoC powder.

$3d_{5/2}$, and Mo^{6+} $3d_{3/2}$, which came into account probably due to the oxidation of Mo_2C surface when exposed to air [50,51]. However, the peaks positioned at 228.8 and 232.4 eV correspond to Mo^{2+} $3d_{5/2}$ and Mo^{2+} $3d_{3/2}$ respectively which are consistent with the carbide phase indicates the presence of Mo_2C. In the case of MoC, the peak positioned at 235.7 eV can be assigned to Mo^{6+} $3d_{3/2}$, whereas the peaks located at 233.5, 232.2, 231.6, and 228.3 eV can be assigned to Mo^{6+} $3d_{5/2}$ (Fig. 4e). The peak observed at 232.8 eV corresponds to Mo^{4+} $3d_{3/2}$ however, the peaks at 229.6 and 228.9 eV correspond to Mo^{4+} $3d_{5/2}$ state (Fig. 4e) [52,53]. The high-resolution spectrum of C1s of Mo_2C and MoC show similar results and are shown in Fig. 4c and f respectively. The high-resolution spectra of C1s can be deconvoluted into three peaks for both the phases. The peaks at 284.2 eV are characteristic of molybdenum bonded carbon [54]. Whereas the peaks at 285.8 and 284.9 can be assigned to C–O and C–C/C=C respectively [31,55]. Finally, Fig. S1a (SI) displays the high-resolution XPS spectra of O1s of Mo_2C. The two peaks located at the binding energies 530.5 and 531.9 represent Mo–O and C–O bonds respectively [51,56]. However, in the case of MoC, the high-resolution spectra of O1s can be deconvoluted into three peaks (Figs. S1b and SI). The peak located at 530.1 eV indicates the presence of Mo–C bond however, the peaks positioned at 230.9 and 232.2 eV confirm the presence of Mo–O bond [53,57,58].

FESEM and EDS

The morphology and elemental analysis of the samples were investigated using FESEM and EDS. The FESEM micrographs of Mo_2C and MoC are shown in Fig. 5a–f respectively. The FESEM images of Mo_2C clearly shows the stacked layered structure of graphitic carbon in which Mo_2C particles are embedded. This provides stability to the structure and contributes to the better electrochemical activity and hence enhances the electrocatalytic performance. The layered structures could also be seen in the FESEM images of MoC shown in Fig. 5d–f. The crystallinity of the graphitic layers seems to be higher than Mo_2C. The structure is more elongated and exhibits faceted to flowery type morphology providing higher surface area. The elemental analysis of the samples was done using Energy Dispersive X-Ray Spectroscopy (EDS). Fig. 5g and h display the EDS results of the Mo_2C and MoC powders respectively. The weight and atomic percentages calculated from the EDS measurements are shown in Table 2. The detected elements are in a good agreement with XRD results. The oxygen was also detected during measurements, which may be expected from surface oxidation of the sample when exposed to air.

TEM

Transmission electron microscopy (TEM) was used to observe the microstructural nature of the synthesized sample. The TEM micrographs of Mo_2C powder are shown in Fig. 6a–d. These micrographs clearly show the spherical shape of the particles. The particle size distribution curve is displayed over Fig. 6a. The average particle size calculated from the Gaussian fit is 33.46 nm, which is greater than the crystallite size estimated from XRD analysis. Fig. 6c and d confirm the insertion of Mo_2C nanoparticles within graphitic carbon layers, which is in good agreement with the XRD results. These micrographs also reveal that the graphitic carbon layers are stacked together and the Mo_2C particles are encapsulated inside the carbon cloth. This type of structure plays a crucial role in the electrochemical activity of the catalyst. The carbon cloth around the Mo_2C particles is responsible to enhance the electrical conductivity of the Mo_2C electrocatalyst [59]. The high-resolution TEM image of the sample indicates the

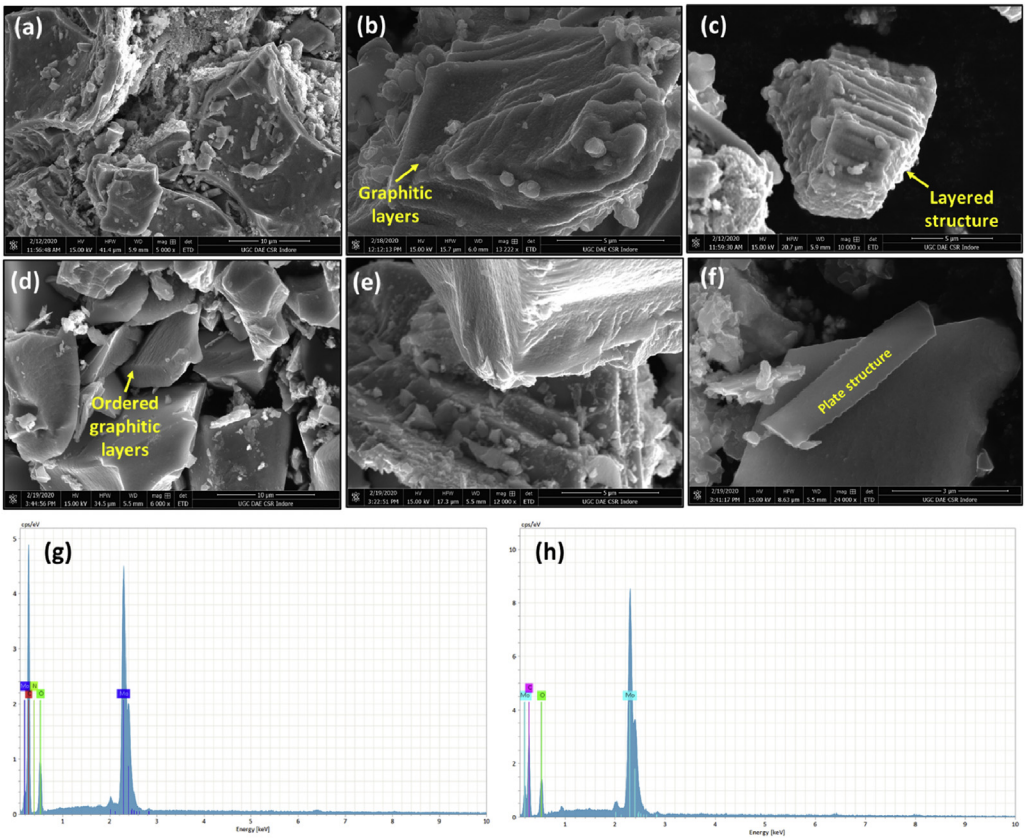

Fig. 5 – (a), (b), (c) FESEM images and (g) EDS of as-synthesized Mo_2C powder; (d), (e), (f) FESEM images and (h) EDS of the MoC powder.

crystalline nature of the powder (Fig. 6e). The interplanar spacing for the (100) plane of Mo_2C was found to be 0.26 nm which is in good agreement with the XRD data. Similarly, the interplanar distances for the planes (101) and (002) were computed to be equal to 0.22 and 0.24 nm respectively. The selected area diffraction pattern (SAED) showed the polycrystalline nature of the as-synthesized Mo_2C powder (Fig. 6f). The interplanar spacing obtained from the SAED pattern was in good agreement with the XRD results. The intense diffraction rings for (101) and (102) planes and weak diffraction rings corresponding to (200), (201) and (203) planes were observed for Mo_2C.

MoC was also investigated by TEM and its micrographs are shown in Fig. 7a–c. The particle size distribution curve is displayed over Fig. 7a. The average particle size was found to be equal to 1.95 nm from Gaussian fit, which is smaller than the Mo_2C particles and the small size may help to enhance the electrochemical properties of the sample. Fig. 7b shows the layered structure of the graphitic carbon, which helps to improve the EDLC performance of the electrocatalyst. The SAED pattern was indexed to (311) and (211) planes of MoC, which confirms the MoC phase as obtained in the XRD results (Fig. 7d).

Table 2 – Elemental composition from EDS measurements.

S. No.	Element	Weight (%)		Atomic (%)	
		Mo_2C	MoC	Mo_2C	MoC
1.	Mo	40.58	44.81	5.83	11.12
2.	C	66.24	31.04	75.99	61.50
3.	O	21.10	18.40	18.18	27.38

Raman

The nature of carbon plays an important role in the conductivity of the sample. To investigate the composition of the as-synthesized Mo_2C powder Raman spectroscopy was conducted and the spectra are shown in Fig. 8. The three characteristic peaks positioned at 663, 820, and 992 cm^{-1} can be attributed to the Mo_2C phase which was observed in XRD results. The two bands at 1364 and 1600 cm^{-1} can be indexed to the D and G band. The MoC powder was also investigated under Raman spectroscopy and the nature of the carbon was found to be similar to Mo_2C. The D and G bands are positioned at 1396 and 1599 cm^{-1}. A small peak at 805.3 cm^{-1} can be indexed to MoC [60]. The D band corresponds to the vibration of sp^3-hybridized carbon atoms representing defect induced structure. However, the G band refers to the sp^2 hybridized carbon type structure [35,51,61]. To determine the nature of graphitization, the intensity ratio of D band to G band (I_D/I_G) plays a crucial role. As this ratio increases the degree of ordering decreases in the carbon material [60,62]. The ratio of the intensity of the D and G band (I_D/I_G) was calculated to be ~0.93 and ~0.85 for Mo_2C and MoC respectively. It indicates the

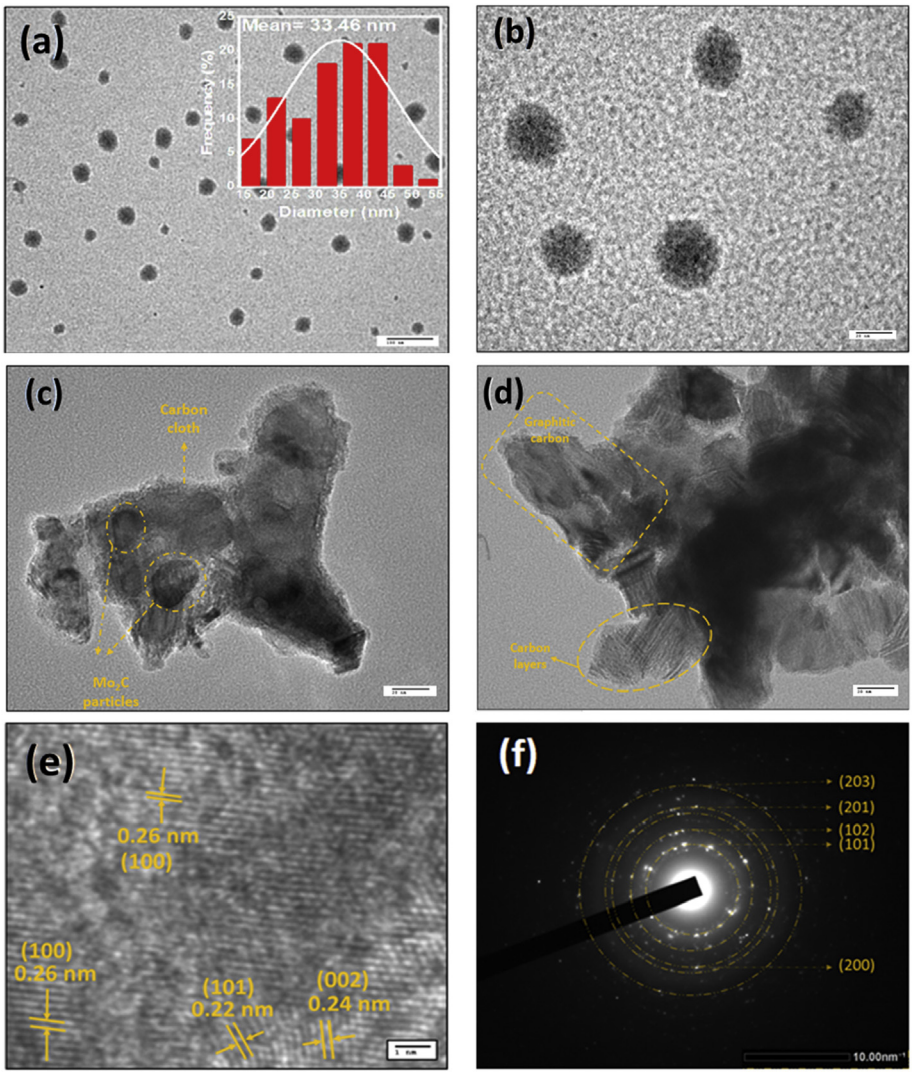

Fig. 6 – (a, b, c, d) TEM micrographs, (e) HRTEM and (f) SAED pattern of the Mo_2C powder.

higher crystallinity of graphitic carbon within MoC than Mo_2C, which is in a good agreement to the FESEM data [63–65].

Electrochemical studies

HER activity

The electrochemical activity of the as-synthesized samples was studied in a three-electrode system using an acidic medium of 0.5 M H_2SO_4. To investigate the HER activity of the as-synthesized samples, linear sweep voltammetry has been performed at a scan rate of 5 mV s^{-1}. The polarization curves of the Mo_2C and MoC in the acidic medium are shown in Fig. 9a. Mo_2C and MoC deliver an overpotential of 260 and 425 mV at a current density of 2 mV cm^{-2} respectively. However, in the case of MoC, the current density decreases sharply with decreasing potential. Also, current fluctuation at lower potential can be observed, which is due to the partially blocked surface area of the electrode by evolved air bubbles during measurements. The electronic structure of Mo_2C is responsible for the higher value of current density. The graphitic carbon on the surface also improves the charge transfer rate on the surface of Mo_2C, which influences the value of current density.

To further investigate the mechanism responsible for HER activity, the Tafel plots were fitted according to the equation $\eta = a + b \log|J|$ where a, b and J are intercept, Tafel slope, and current density respectively. The HER mechanism involves the following pathways [36,64].

Step I: $M + H_3O^+ + e^- \leftrightarrow MH_{ads} + H_2O$ (Volmer reaction)

Step II: $MH_{ads} + H_3O^+ + e^- \leftrightarrow H_2 + M + H_2O$ (Heyrovsky reaction)

Step III: $MH_{ads} + MH_{ads} \leftrightarrow H_2 + 2M$ (Tafel reaction)

Here M is the active site and MH_{ads} denote the hydrogen adsorbed on that active site. If the value of the Tafel slope is about 40 and 30 mV dec^{-1} then Heyrovsky and Tafel reactions determine the rate of the reaction. The rate-determining step will be the Volmer reaction when the value of the Tafel slope is

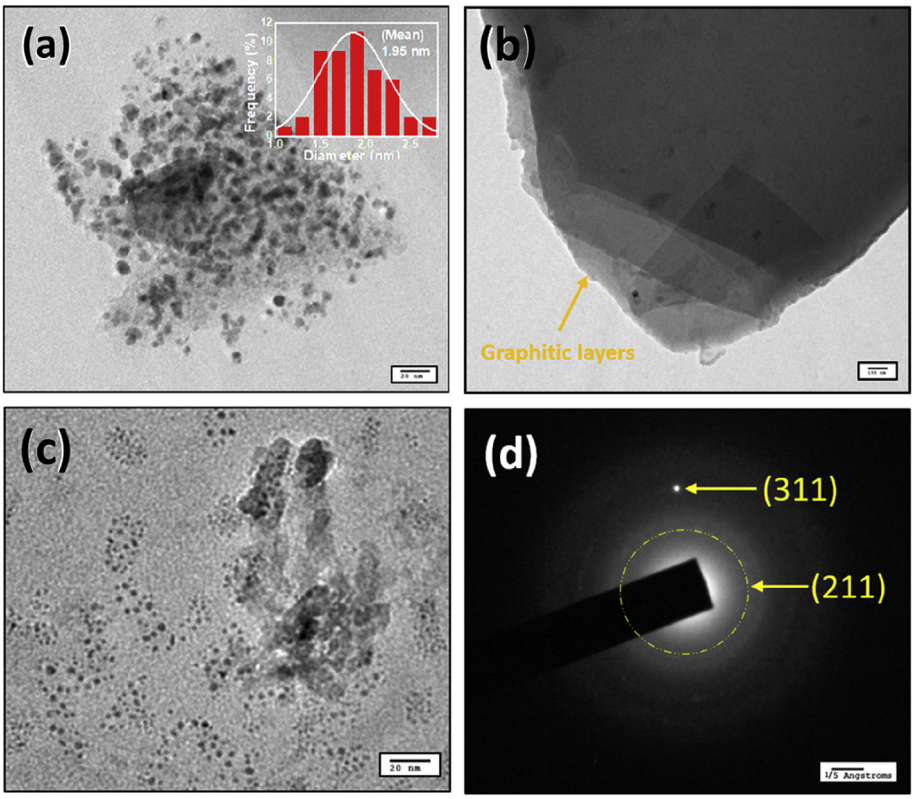

Fig. 7 – (a, b, c) TEM micrographs and (d) SAED pattern of the as-synthesized MoC powder.

up to 120 mV dec^{-1}. The Tafel plots of both the samples are displayed in Fig. 9b. The Tafel slope of 129.7 mV dec^{-1} was obtained for Mo_2C however, MoC shows a Tafel slope of 266 mV dec^{-1}. This indicates that the Mo_2C phase of molybdenum carbide is more suitable for hydrogen evolution reaction because of its platinum-like electronic structure. The Tafel slope of both the samples suggests that the rate-determining step is the Volmer reaction. The higher value of b for MoC indicates the faster reaction kinetics on the surface of it. The synthesized Mo_2C powder exhibits a small Tafel slope (129.7 mV dec^{-1}) which means that it is one of the best Mo-based electrocatalysts than other reported work as given in Table S1 (SI).

Electrochemical double-layer capacitance (EDLC, C_{dl})

To investigate the electrochemical double-layer capacitance (EDLC, C_{dl}) CV measurements were done which were performed in a voltage range of 0–0.4 V at various scan rates ranging from 5 to 250 mV/s. The CV plots of Mo_2C and MoC at different scan rates are displayed in Fig. 10a and b respectively. The plots between scan rates (mV sec^{-1}) versus current density $\Delta j_{0.2}$ (mA cm^{-2}) of Mo_2C and MoC are shown in Fig. 10c.

MoC and Mo_2C showed a C_{dl} value of 8.99 and 2.47 mF cm^{-2} respectively which is consistent with the literature [48]. The higher C_{dl} value of MoC suggests that it can be a suitable candidate for high-performance capacitors. The particle size plays an important role in the electrochemical capacitance of the sample. The smaller the size of the particle the higher will be its capacitance [66]. The pure phase Mo_2C showed a sharp rectangular-shaped CV plot, which indicates high electrochemical reversibility during charging-discharging cycles even at higher scan rates. MoC shows a rectangular-shaped CV cycle exhibiting a large value of charge storage capacity. The larger value of C_{dl} for MoC might be a result of fast charge separation of non-faradic processes within the electrolyte and electrode interface. The specific capacitance measured from the CV plots at multiple scan rates for Mo_2C and MoC were found to be equal to 2.24 mF g^{-1} and 8.17 mF g^{-1} respectively. In the case of MoC, two weak redox peaks can be observed at lower scan rates, which indicates the presence of an additional pseudocapacitive behavior along with EDLC [67]. These

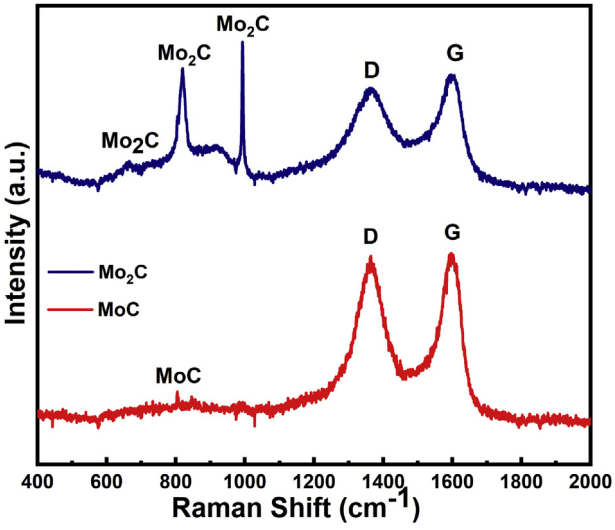

Fig. 8 – Raman spectra of as-synthesized Mo_2C and MoC powders.

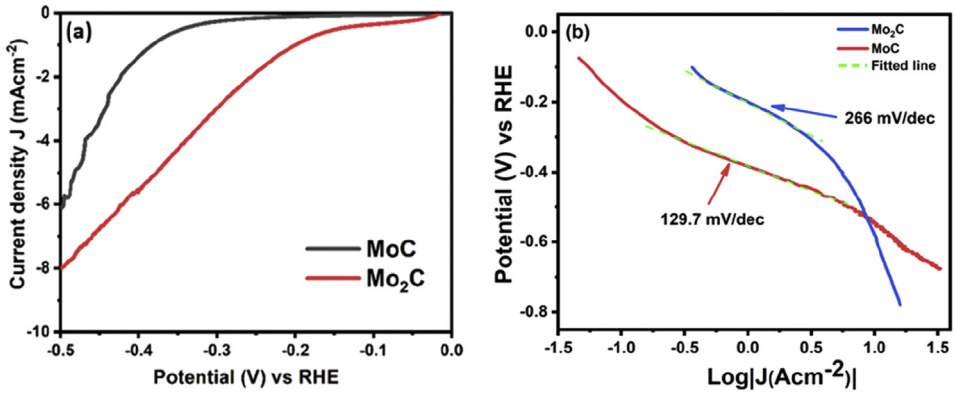

Fig. 9 – (a) LSV curves and (b) Tafel plots of the as-prepared Mo_2C and MoC powders.

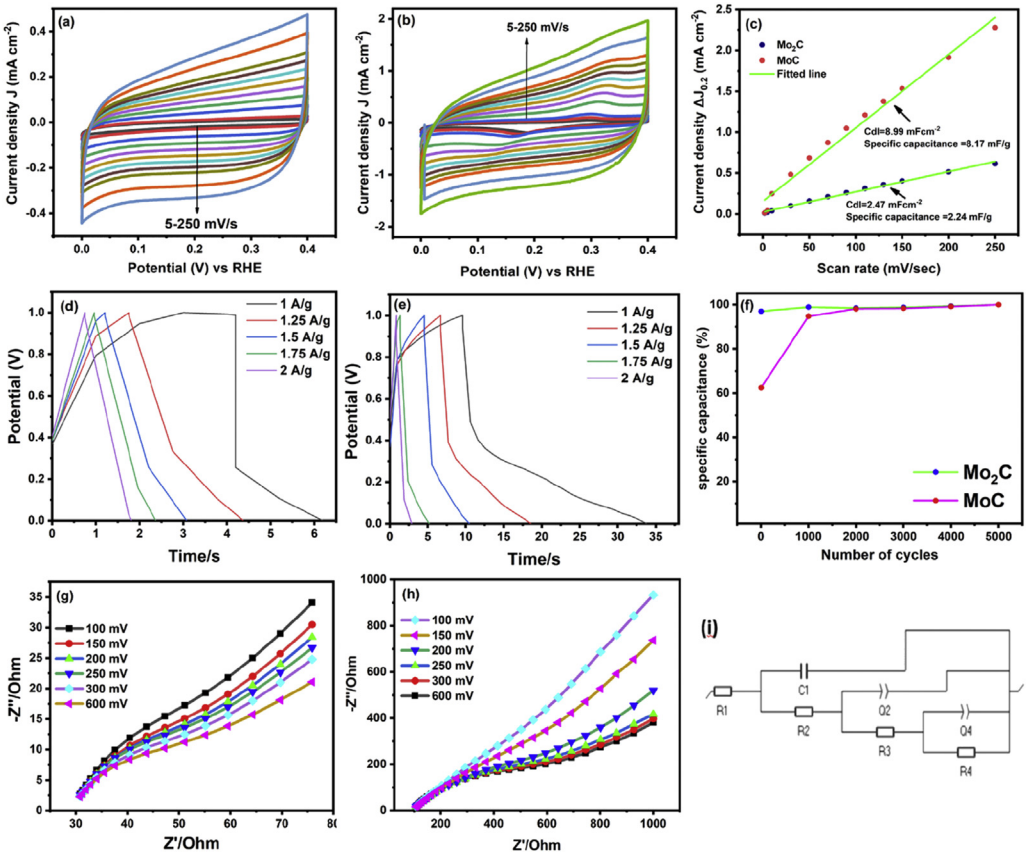

Fig. 10 – Cyclic voltammetry curves at different scan rates of (a) Mo_2C and (b) MoC; (c) scan rates vs. current density ($\Delta J_{0.2}$) curves of Mo_2C and MoC; GCD curves of (d) Mo_2C and (e) MoC powder; (f) number of cycles vs. specific capacitance (%) of Mo_2C and MoC powder; EIS curves of (g) Mo_2C and (h) MoC powder; (i) Z-fitted equivalent circuit of EIS curves of Mo_2C and MoC.

redox peaks weaken at higher scan rates which are due to greater polarization as the potential of the redox reaction exceeds the scan potential range [68]. The galvanostatic charge-discharge measurements were also done to confirm the capacitive behavior of the samples as indicated by CV data. All the GCD measurements were performed in 0.5 M H_2SO_4 at different current densities ranging from 1 to 2 A g^{-1}. The discharge time and specific capacitance of the electrode are directly related to each other by the relation,

$$C(F/g) = \frac{I \times \Delta t}{\Delta V \times m} \quad (5)$$

Where I denote the discharge current, Δtis the discharge time, ΔVrepresents the potential window and m is the mass of the catalyst. The charge-discharge curves of Mo_2C and MoC are shown in Fig. 10d and e respectively. The charging time of both the samples is approximately the same. However, MoC shows a higher discharge time, which indicates the higher

specific capacitance of MoC as they are directly proportional to each other. With increasing current density, the discharge time decreases which indicates the decrement in specific capacitance. This could be due to the shortage of time available for the ions of the electrolyte to disperse on the sample surface. These results are in good agreement with the CV measurements.

Another key factor of an electrocatalyst is long-term stability. To evaluate the stability of the synthesized powders, CV measurements were performed in a voltage range of 0–0.4 V at a scan rate of 100 mV/s for 5000 cycles, which took 10 h to complete. The graphs between the number of cycles and percentage specific capacitance for Mo_2C and MoC are shown in Fig. 10f. Also, The CV plots obtained for both the phases up to 5000 cycles are shown in Fig. S2 (SI). CV curves of Mo_2C are displayed in Fig. S2a however, Fig. S2b shows the CV curves of MoC. For Mo_2C, the CV curves nearly remain the same up to 5000 CV cycles, which indicates that it is very stable HER electrocatalyst in acidic medium. The high stability may be due to the graphitic carbon on the surface of Mo_2C particles. In the case of MoC, the shape of the CV curves changes during the first 2000 cycles, and after that, the shape of the CV curves remains approximately the same up to 5000 cycles. The poor stability may be due to the less carbon amount in MoC which suggests that it is not stable HER electrocatalyst.

Electrochemical impedance spectroscopy (EIS)

The Mo_2C and MoC powder were further investigated with EIS to get more information about the interfacial properties of the obtained catalysts in 0.5 M H_2SO_4. The information about the reaction kinetics and the adsorption/desorption on the catalyst surface can be gathered from the EIS curves. The typical Nyquist plots of Mo_2C and MoC from the EIS measurements at various overpotentials ranging from 100 to 600 mV are displayed in Fig. 10. The Nyquist curves of Mo_2C are displayed in Fig. 10g, however, Fig. 10h shows the Nyquist curves of MoC. Fig. 10i shows the electrical equivalent circuit model of both the phases by Z-fitting of the EIS curves. The charge transfer resistance ($R_1 = R_{ct}$) values were calculated from the Nyquist plots at 200 mV to compare charge transfer kinetics of both the phases. The Nyquist plots revealed that the R_{ct} value of Mo_2C (26.37 Ω) is obviously lower than that of MoC (88.91 Ω), which indicates the high efficiency and fastest electron transfer of Mo_2C during HER. The Nyquist plots of Mo_2C at different overpotentials reveal that the R_{ct} values decrease with increasing overpotentials from 29.45 Ω at 100 mV to 22.49 Ω at 600 mV. This indicates the fast reaction rate and favorable behavior of charge transfer kinetics towards HER [69]. For MoC, the R_{ct} values at 100 mV and 600 mV are 90.25 and 84.72 Ω respectively, which are similar to Mo_2C.

Conclusion

In summary, we reported carbon-coated Mo_2C and MoC phases of molybdenum carbide, synthesized in a stainless-steel autoclave at a temperature of 800 °C for 8 (1:12; Mo:C) and 15 h (1:10; Mo:C) respectively. The synthesis temperature, reaction time, and molar ratio of precursors play an important role in the synthesis of pure phase molybdenum carbides. The results indicate that pure phase Mo_2C and MoC can be produced under similar conditions just varying the reaction parameters. The results show that Mo_2C is encapsulated inside graphitic carbon layers and has a stacked layered structure. The particle and crystallite size of MoC are lower than that of Mo_2C, which increases its capability to store energy. However, Mo_2C shows higher HER activity due to its Pt like electronic structure. Mo_2C shows a low value of specific capacitance because of its large particle and crystallite size. The graphitic layers provide a path to the electrons and electrolyte ions to interact with the electrocatalyst (Mo_2C) and hence increases its activity. The carbon matrix enhances the stability of the electrocatalyst, which is a critical factor of an electrocatalyst to be useful. The high specific capacitance value of MoC calculated from EDLC measurements suggests its broad application in energy storage devices. Mo_2C exhibits high stability however, MoC shows poor stability towards HER up to 5000 CV cycles. The synthesis of a noble metal-free catalyst via the aforementioned method can be an effective and environment-friendly way to achieve pure phase Mo_2C and MoC at different reaction conditions.

Declaration of competing interest

The authors declare that they have no known competing financial interests or personal relationships that could have appeared to influence the work reported in this paper.

Acknowledgment

The authors are highly thankful to Dr. Uday Deshpande (Scientist-E), XPS lab, UGC-DAE CSR Indore for XPS analysis. Authors express special gratitude to Dr. Vasant Sathe (Scientist-G), Raman lab, and Dr. R. Venkatesh (Scientist-E), FESEM lab, UGC-DAE CSR Indore for Raman and FESEM measurements. The authors offer special thanks to SAI lab, Thapar Institute of Engineering and Technology, Patiala for XRD analysis. The authors are grateful to Mr. Manu Vashishtha, AIRF-JNU, New Delhi for TEM/HRTEM analysis. This work was supported by UGC-DAE Consortium for Scientific Research (project no.- CSR-IC-239/2017-18/1320) Indore, India. The authors are thankful to the Co-PI of this project Dr. N.P. Lalla (Scientist-H), UGC-DAE CSR Indore for the assistance in characterizations.

Appendix A. Supplementary data

Supplementary data to this article can be found online at https://doi.org/10.1016/j.ijhydene.2020.07.069.

REFERENCES

[1] Shi Y, Zhang B. Recent advances in transition metal phosphide nanomaterials: synthesis and applications in

hydrogen evolution reaction. Chem Soc Rev 2016;45:1529–41. https://doi.org/10.1039/c5cs00434a.
[2] Laursen AB, Patraju KR, Whitaker MJ, Retuerto M, Sarkar T, Yao N, et al. Nanocrystalline Ni_5P_4: a hydrogen evolution electrocatalyst of exceptional efficiency in both alkaline and acidic media. Energy Environ Sci 2015;8:1027–34. https://doi.org/10.1039/c4ee02940b.
[3] Lu Q, Hutchings GS, Yu W, Zhou Y, Forest RV, Tao R, et al. Highly porous non-precious bimetallic electrocatalysts for efficient hydrogen evolution. Nat Commun 2015;6:6567. https://doi.org/10.1038/ncomms7567.
[4] Hui L, Xue Y, Yu H, Liu Y, Fang Y, Xing C, et al. Highly efficient and selective generation of ammonia and hydrogen on a graphdiyne-based catalyst. J Am Chem Soc 2019;141:10677–83. https://doi.org/10.1021/jacs.9b03004.
[5] Zhuo J, Wang T, Zhang G, Liu L, Gan L, Li M. Salts of $C_{60}(OH)_8$ electrodeposited onto a glassy carbon electrode: surprising catalytic performance in the hydrogen evolution reaction. Angew Chem Int Ed 2013;52:10867–70. https://doi.org/10.1002/anie.201305328.
[6] Xu YF, Gao MR, Zheng YR, Jiang J, Yu SH. Nickel/nickel(II) oxide nanoparticles anchored onto cobalt(IV) diselenide nanobelts for the electrochemical production of hydrogen. Angew Chem Int Ed 2013;52:8546–50. https://doi.org/10.1002/anie.201303495.
[7] Morales-Guio CG, Stern LA, Hu X. Nanostructured hydrotreating catalysts for electrochemical hydrogen evolution. Chem Soc Rev 2014;43:6555–69. https://doi.org/10.1039/c3cs60468c.
[8] Liu Q, Tian J, Cui W, Jiang P, Cheng N, Asiri AM, et al. Carbon nanotubes decorated with CoP nanocrystals: a highly active non-noble-metal nanohybrid electrocatalyst for hydrogen evolution. Angew Chem Int Ed 2014;53:6710–4. https://doi.org/10.1002/anie.201404161.
[9] Li X, Zhang R, Luo Y, Liu Q, Lu S, Chen G, et al. Cobalt-phosphorous nanoparticles decorated N-doped carbon nanosheet array for efficient and durable hydrogen evolution at alkaline pH. Sustain Energy Fuels 2020. https://doi.org/10.1039/d0se00240b.
[10] Guo Y, Tang J, Wang Z, Kang YM, Bando Y, Yamauchi Y. Elaborately assembled core-shell structured metal sulfides as a bifunctional catalyst for highly efficient electrochemical overall water splitting. Nano Energy 2018;47:494–502. https://doi.org/10.1016/j.nanoen.2018.03.012.
[11] Guo Y, Park T, Yi JW, Henzie J, Kim J, Wang Z, et al. Nanoarchitectonics for transition-metal-sulfide-based electrocatalysts for water splitting. Adv Mater 2019;31:1–34. https://doi.org/10.1002/adma.201807134.
[12] Liu T, Liu D, Qu F, Wang D, Zhang L, Ge R, et al. Enhanced electrocatalysis for energy-efficient hydrogen production over CoP catalyst with nonelectroactive Zn as a promoter. Adv Energy Mater 2017;7. https://doi.org/10.1002/aenm.201700020.
[13] Sawhill SJ, Layman KA, Van Wyk DR, Engelhard MH, Wang C, Bussell ME. Thiophene hydrodesulfurization over nickel phosphide catalysts: effect of the precursor composition and support. J Catal 2005;231:300–13. https://doi.org/10.1016/j.jcat.2005.01.020.
[14] Tang C, Pu Z, Liu Q, Asiri AM, Sun X. NiS_2 nanosheets array grown on carbon cloth as an efficient 3D hydrogen evolution cathode. Electrochim Acta 2015;153:508–14. https://doi.org/10.1016/j.electacta.2014.12.043.
[15] Chen WF, Sasaki K, Ma C, Frenkel AI, Marinkovic N, Muckerman JT, et al. Hydrogen-evolution catalysts based on non-noble metal nickel-molybdenum nitride nanosheets. Angew Chem Int Ed 2012;51:6131–5. https://doi.org/10.1002/anie.201200699.
[16] Fan C. Study of electrodeposited nickel-molybdenum, nickel-tungsten, cobalt-molybdenum, and cobalt-tungsten as hydrogen electrodes in alkaline water electrolysis. J Electrochem Soc 1994;141:382. https://doi.org/10.1149/1.2054736.
[17] Wu L, Pu Z, Tu Z, Amiinu IS, Liu S, Wang P, et al. Integrated design and construction of WP/W nanorod array electrodes toward efficient hydrogen evolution reaction. Chem Eng J 2017;327:705–12. https://doi.org/10.1016/j.cej.2017.06.152.
[18] Xiao P, Yan Y, Ge X, Liu Z, Wang JY, Wang X. Investigation of molybdenum carbide nano-rod as an efficient and durable electrocatalyst for hydrogen evolution in acidic and alkaline media. Appl Catal B Environ 2014;154–155:232–7. https://doi.org/10.1016/j.apcatb.2014.02.020.
[19] Vrubel H, Hu X. Molybdenum boride and carbide catalyze hydrogen evolution in both acidic and basic solutions. Angew Chem Int Ed 2012;51:12703–6. https://doi.org/10.1002/anie.201207111.
[20] Liu B, Wang S, Mo Q, Peng L, Cao S, Wang J, et al. Epitaxial MoS_2 nanosheets on nitrogen doped graphite foam as a 3D electrode for highly efficient electrochemical hydrogen evolution. Electrochim Acta 2018;292:407–18. https://doi.org/10.1016/j.electacta.2018.09.160.
[21] Mao X, Zou J, Li D, Zhao G, Song Z. Applied Surface Science $MoSe_2$/graphite composite with excellent hydrogen evolution reaction performance fabricated by rapid selenization method. Appl Surf Sci 2019;471:142–8. https://doi.org/10.1016/j.apsusc.2018.11.189.
[22] Giordano C, Erpen C, Yao W, Antonietti M. Synthesis of Mo and W carbide and nitride nanoparticles via a simple "urea glass" route. Nano Lett 2008;8:4659–63. https://doi.org/10.1021/nl8018593.
[23] Wang Y, Senthil RA, Pan J, Sun Y, Osman S, Khan A. Facile construction of N-doped Mo_2C@CNT composites with 3D nanospherical structures as an efficient electrocatalyst for hydrogen evolution reaction. Int J Ionics Sci Technol Ion Motion 2019;25:4273–83. https://doi.org/10.1007/s11581-019-02985-8.
[24] Wu HBin, Xia BY, Yu L, Yu X-Y, (David) Lou XW. Porous molybdenum carbide nano-octahedrons synthesized via confined carburization in metal-organic frameworks for efficient hydrogen production. Nat Commun 2015;6:6512. https://doi.org/10.1038/ncomms7512.
[25] Anjum MAR, Lee MH, Lee JS. BCN network-encapsulated multiple phases of molybdenum carbide for efficient hydrogen evolution reactions in acidic and alkaline media. J Mater Chem A 2017;5:13122–9. https://doi.org/10.1039/c7ta03407e.
[26] Lin H, Shi Z, He S, Yu X, Wang S, Gao Q, et al. Heteronanowires of MoC-Mo_2C as efficient electrocatalysts for hydrogen evolution reaction. Chem Sci 2016;7:3399–405. https://doi.org/10.1039/c6sc00077k.
[27] Politi JRDS, Viñes F, Rodriguez JA, Illas F. Atomic and electronic structure of molybdenum carbide phases: bulk and low Miller-index surfaces. Phys Chem Chem Phys 2013;15:12617–25. https://doi.org/10.1039/c3cp51389k.
[28] Zhang K, Li C, Zhao Y, Yu X, Chen Y. Porous one-dimensional Mo_2C-amorphous carbon composites: high-efficient and durable electrocatalysts for hydrogen generation. Phys Chem Chem Phys 2015;17:16609–14. https://doi.org/10.1039/c5cp02028j.
[29] Ma R, Zhou Y, Chen Y, Li P, Liu Q, Wang J. Ultrafine molybdenum carbide nanoparticles composited with carbon as a highly active hydrogen-evolution electrocatalyst. Angew Chem Int Ed 2015;54:14723–7. https://doi.org/10.1002/anie.201506727.
[30] Mu Y, Zhang Y, Fang L, Liu L, Zhang H, Wang Y. Controllable synthesis of molybdenum carbide nanoparticles embedded in porous graphitized carbon matrixes as efficient electrocatalyst for hydrogen evolution reaction. Electrochim

Acta 2016;215:357–65. https://doi.org/10.1016/j.electacta.2016.08.104.
[31] Dong J, Wu Q, Huang C, Yao W, Xu Q. Cost effective Mo rich Mo_2C electrocatalysts for the hydrogen evolution reaction. J Mater Chem A 2018;6:10028–35. https://doi.org/10.1039/c8ta02550a.
[32] Zhao Y, Wang S, Liu H, Guo X, Zeng X, Wu W, et al. Porous Mo_2C nanorods as an efficient catalyst for the hydrogen evolution reaction. J Phys Chem Solids 2019;132:230–5. https://doi.org/10.1016/j.jpcs.2019.05.003.
[33] Pan Lin Feng, Li Yu Hang, Yang Shuang, Liu Peng Fei, Yu MQ, Yang HG. Molybdenum carbide stabilized on graphene with high electrocatalytic activity for hydrogen evolution reaction †. Chem Commun 2014;50:13135–7. https://doi.org/10.1039/C4CC05698A.
[34] Xia K, Guo J, Xuan C, Huang T, Deng Z, Chen L, et al. Ultrafine molybdenum carbide nanoparticles supported on nitrogen doped carbon nanosheets for hydrogen evolution reaction. Chinese Chem Lett 2019;30:192–6. https://doi.org/10.1016/j.cclet.2018.05.009.
[35] Huang Y, Gong Q, Song X, Feng K, Nie K, Zhao F, et al. Mo_2C nanoparticles dispersed on hierarchical carbon microflowers for efficient electrocatalytic hydrogen evolution. ACS Nano 2016;10:11337–43. https://doi.org/10.1021/acsnano.6b06580.
[36] Šljukić B, Vujković M, Amaral L, Santos DMF, Rocha RP, Sequeira CAC, et al. Carbon-supported Mo_2C electrocatalysts for hydrogen evolution reaction. J Mater Chem A 2015;3:15505–12. https://doi.org/10.1039/c5ta02346g.
[37] Cao Q, Zhao L, Wang A, Yang L, Lai L, Wang ZL, et al. Tailored synthesis of Zn-N co-doped porous MoC nanosheets towards efficient hydrogen evolution. Nanoscale 2019;11:1700–9. https://doi.org/10.1039/c8nr07463a.
[38] Yan Z, He G, Shen K, Luo Z. MoC–graphite composite as a Pt electrocatalyst support for highly active methanol oxidation and oxygen reduction reaction. J Mater Chem A 2014;2:4014–22. https://doi.org/10.1039/c3ta14251e.
[39] Zhang Y, Li C, Chen Z, Ni Y, Kong F, Kong A, et al. Ionic liquid-derived MoC nanocomposites with ordered mesoporosity as efficient Pt-free electrocatalyst for hydrogen evolution and oxygen reduction. Catal Lett 2017;147:253–60. https://doi.org/10.1007/s10562-016-1914-3.
[40] Yang Li, Huang Qilin, Wu Hongbiao, Cai Lun, Du Yiming, Liu Shiqiu, Sheng Z, Wu M. N-doped Mo_2C nanoblock for efficient hydrogen evolution reaction. J Solid State Electrochem 2019;23:2043–50. https://doi.org/10.1007/s10008-019-04302-9.
[41] Cui W, Cheng N, Liu Q, Ge C, Asiri AM, Sun X. Mo_2C nanoparticles decorated graphitic carbon sheets: biopolymer-derived solid-state synthesis and application as an efficient electrocatalyst for hydrogen generation. ACS Catal 2014;4:2658–61. https://doi.org/10.1021/cs5005294.
[42] Tang Y, Li W, Jiao L, Li F, Yang Y, Wang X, et al. Mo_2C-Ni-modified nitrogen-doped carbon nanofiber toward efficient hydrogen evolution reaction. New J Chem 2017;41:12956–61. https://doi.org/10.1039/c7nj02611k.
[43] Lv C, Wang J, Huang Q, Yang Q, Huang Z, Zhang C. Facile synthesis of hollow carbon microspheres embedded with molybdenum carbide nanoparticles as an efficient electrocatalyst for hydrogen generation. RSC Adv 2016;6:75870–4. https://doi.org/10.1039/c6ra16490k.
[44] He C, Tao J. Two-dimensional TaC nanosheets on a reduced graphene oxide hybrid as an efficient and stable electrocatalyst for water splitting. Chem Commun 2016;52:8810–3. https://doi.org/10.1039/c6cc03876j.
[45] Saghafi M, Heshmati-Manesh S, Ataie A, Khodadadi AA. Synthesis of nanocrystalline molybdenum by hydrogen reduction of mechanically activated MoO_3. Int J Refract Met Hard Mater 2012;30:128–32. https://doi.org/10.1016/j.ijrmhm.2011.07.014.
[46] Sambalova O, Hany R, Jenatsch S, Delmelle R, Nüesch F, Borgschulte A. Hydrogen reduction of molybdenum oxide at room temperature. Sci Rep 2017;7:1–9. https://doi.org/10.1038/srep40761.
[47] Mir RA, Pandey OP. Influence of graphitic/amorphous coated carbon on HER activity of low temperature synthesized B-Mo_2C@C nanocomposites. Chem Eng J 2018;348:1037–48. https://doi.org/10.1016/j.cej.2018.05.041.
[48] Mir RA, Pandey OP. Influence of graphitic/amorphous coated carbon on HER activity of low temperature synthesized β-Mo_2C@C nanocomposites. Chem Eng J 2018;348:1037–48. https://doi.org/10.1016/j.cej.2018.05.041.
[49] Wu C, Li J. Unique hierarchical Mo_2C/C nanosheet hybrids as active electrocatalyst for hydrogen evolution reaction. ACS Appl Mater Interfaces 2017;9:41314–22. https://doi.org/10.1021/acsami.7b13822.
[50] Fan X, Liu Y, Peng Z, Zhang Z, Zhou H, Zhang X, et al. Atomic H-induced Mo_2C hybrid as an active and stable bifunctional electrocatalyst. ACS Nano 2017;11:384–94. https://doi.org/10.1021/acsnano.6b06089.
[51] Li R, Wang S, Wang W, Cao M. Ultrafine Mo_2C nanoparticles encapsulated in N-doped carbon nanofibers with enhanced lithium storage performance †. Phys Chem Chem Phys 2015;17:24803–9. https://doi.org/10.1039/C5CP03890A.
[52] Wan C, Regmi YN, Leonard BM. Multiple phases of molybdenum carbide as electrocatalysts for the hydrogen evolution reaction. Angew Chem 2014;126:6525–8. https://doi.org/10.1002/ange.201402998.
[53] NIST X-ray Photoelectron Spectroscopy Database. NIST Standard Reference Database Number 20. Gaithersburg MD: National Institute of Standards and Technology; 2000. p. 20899. n.d. https://srdata.nist.gov/xps/.
[54] Zhu Y, Wang S, Zhong Y, Cai R, Li L. Facile synthesis of a MoO_2-Mo_2C-C composite and its application as favorable anode material for lithium-ion batteries. J Power Sources 2016;307:552–60. https://doi.org/10.1016/j.jpowsour.2016.01.014.
[55] Bazylewski P, Boukhvalov DW, Kukharenko AI, Kurmaev EZ, Hunt A. The characterization of Co-nanoparticles supported on graphene. RSC Adv 2015;5:75600–6. https://doi.org/10.1039/C5RA12893E.
[56] Gao W, Shi Y, Zhang Y, Zuo L, Lu H, Huang Y, et al. Molybdenum carbide anchored on graphene nanoribbons as highly efficient all-pH hydrogen evolution reaction electrocatalyst. ACS Sustain Chem Eng 2016;4:6313–21. https://doi.org/10.1021/acssuschemeng.6b00859.
[57] Nishanthi ST, Baruah A, Yadav KK, Sarker D, Ghosh S, Ganguli AK, et al. New low temperature environmental friendly process for the synthesis of tetragonal MoO_2 and its field emission properties. Appl Surf Sci 2019;467–468:1148–56. https://doi.org/10.1016/j.apsusc.2018.10.173.
[58] Saha A, Paul A, Srivastava DN, Panda AB. Porous carbon incorporated β-Mo_2C hollow sphere: an efficient electrocatalyst for hydrogen evolution reaction. Int J Hydrogen Energy 2018;43:21655–64. https://doi.org/10.1016/j.ijhydene.2018.04.051.
[59] Wu C, Dong G, Guan L. Production of graphene sheets by a simple helium arc-discharge. Phys E Low Dimens Syst Nanostruct 2010;42:1267–71. https://doi.org/10.1016/j.physe.2009.10.054.
[60] Li M, Yu S, Chen Z, Wang Z, Lv F, Nan B, et al. MoC ultrafine nanoparticles confined in porous graphitic carbon as extremely stable anode materials for lithium- and sodium-ion batteries. Inorg Chem Front 2017;4:289–95. https://doi.org/10.1039/c6qi00465b.
[61] Wang D, Wang J, Luo X, Wu Z, Ye L. In situ preparation of Mo_2C nanoparticles embedded in ketjenblack carbon as

highly efficient electrocatalysts for hydrogen evolution. ACS Sustain Chem Eng 2018;6:983–90. https://doi.org/10.1021/acssuschemeng.7b03317.

[62] Liu HJ, Cui WJ, Jin LH, Wang CX, Xia YY. Preparation of three-dimensional ordered mesoporous carbon sphere arrays by a two-step templating route and their application for supercapacitors. J Mater Chem 2009;19:3661–7. https://doi.org/10.1039/b819820a.

[63] Lv C, Huang Z, Yang Q, Wei G, Chen Z, Humphrey MG, et al. Ultrafast synthesis of molybdenum carbide nanoparticles for efficient hydrogen generation. J Mater Chem A 2017;5:22805–12. https://doi.org/10.1039/c7ta06266d.

[64] Sen Li J, Wang Y, Liu CH, Li SL, Wang YG, Dong LZ, et al. Coupled molybdenum carbide and reduced graphene oxide electrocatalysts for efficient hydrogen evolution. Nat Commun 2016;7:1–8. https://doi.org/10.1038/ncomms11204.

[65] Pu Z, Wang M, Kou Z, Amiinu IS, Mu S. Mo_2C quantum dot embedded chitosan-derived nitrogen-doped carbon for efficient hydrogen evolution in a broad pH range. Chem Commun 2016;52:12753–6. https://doi.org/10.1039/c6cc06267a.

[66] Jayalakshmi M, Mohan Rao M, Kim KB. Effect of particle size on the electrochemical capacitance of α-Ni(OH)2 in alkali solutions. Int J Electrochem Sci 2006;1:324–33.

[67] Hong X, Fu J, Liu Y, Li S, Wang X, Dong W, et al. Recent progress on graphene/polyaniline composites for high-performance supercapacitors. Mater (Basel, Switzerland) 2019;12. https://doi.org/10.3390/ma12091451.

[68] Qiu B, Wang J, Li Z, Wang X, Li X. Influence of acidity and oxidant concentration on the nanostructures and electrochemical performance of polyaniline during fast microwave-assisted chemical polymerization. Polymers (Basel) 2020;12:310. https://doi.org/10.3390/polym12020310.

[69] Zhou W, Xiong T, Shi C, Zhou J, Zhou K, Zhu N, et al. Bioreduction of precious metals by microorganism: efficient gold@N-doped carbon electrocatalysts for the hydrogen evolution reaction. Angew Chem Int Ed 2016;55:8416–20. https://doi.org/10.1002/anie.201602627.